DirectHop: A Direct-Drive Insect-Sized Robot that can Control Jump Height and Self-Right

Hanquan Wang[1], Yash P. Talwekar[1], Sawyer B. Fuller[1,2]

***Abstract*— Insect-scale jumping robots are low-cost, agile, and have the potential to be powered by harvested energy. To date, most electrically powered jumping robots actuate by releasing a spring. However, the increased jump height enabled by springs is not needed for many applications, and it increases complexity. Direct actuation, on the other hand, allows jump distance to be easily controlled, mimicking the versatility of many larger biological jumpers. Here we present DirectHop, a 1.0 g, 50 mm robot inspired by this principle. It uses a coreless direct current (DC) motor, pulley, and micromachined carbon fiber composite sarrus linkage to directly actuate its jump. We show that jump height can be precisely and repeatedly controlled, allowing for more precise location control. With a 45° ramp under the foot, it can surmount a standard 17 cm high stair step, which makes it suitable for mobility in urban environments. DirectHop self-rights with a 90% first-try success rate using a process mediated by a roll cage and active retraction. This has enabled up to four sequential jumps. The upper bound of electromechanical efficiency is 39.0%, giving a projected 18 J/m/kg Cost of Transport (CoT) using the mean center of mass (CoM) height. This is nearly two orders of magnitude lower than flying robots, the only other class of robots at this scale capable of climbing stairs.**

I. Introduction

The extraordinary agility and robustness of biological organisms has long served as a primary inspiration for the design of microrobots. Biological jumpers operate across different paradigms depending on their scale [1]. At the micro-scale, organisms like fleas and froghoppers utilize elastic energy storage to exceed the instantaneous power limits of muscle tissue, jumping hundreds of times their body length [2], [3]. Larger organisms such as frogs and locusts rely primarily on direct muscle contraction, a paradigm that affords them the ability to vary jump height over a continuously-variable range.

Replicating impulsive performance in engineered systems 1 g and below has almost exclusively relied on the "store-and-release" approach analogous to micro-scale insects [4], [5], [6], [1]. These systems actuate using work multiplication, slowly storing energy into an elastic element with a low-power actuator and then releasing it suddenly to produce large jumps [1]. Two recent advancements exemplify the tradeoffs of this approach. At one extreme, an all-or-nothing jumper obtained a substantial jump of over 30 m, as well as self-reloading and self-righting, but without control of height [1]. At the other extreme, a careful design of a latch

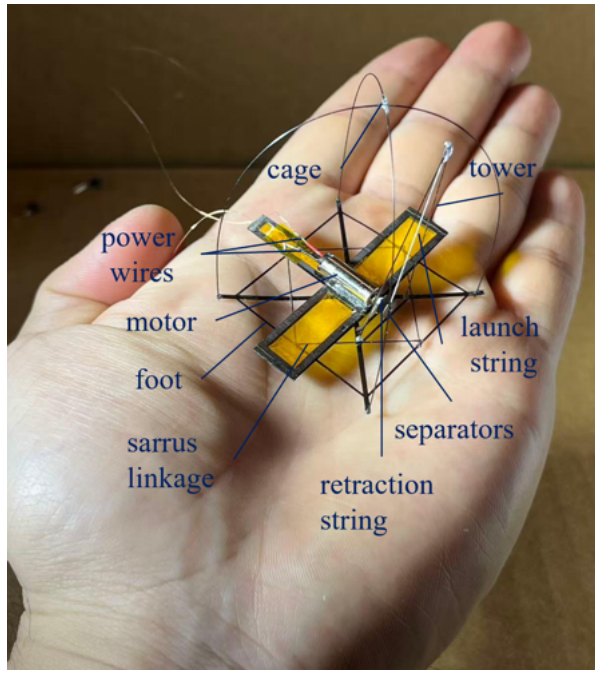

Fig. 1. **The** $1.0\,\mathrm{g}$ **hopping and self-righting system.** It consists of a coreless direct-current (DC) motor that actuates in direct drive mode, using a pulley and string to lift itself against a rigid tower. A laser-microfabricated carbon fiber sarrus linkage constrains the motor to translational motion to minimize rotation during the aerial phase. Retraction and self-righting is performed by reversing the motor to pull on the retraction string on the same pulley. A protective roll cage stabilizes orientation onto the foot. Separators on the pulley between the two strings prevent entanglement.

system with a curved release allowed modulating the jump on a 4 g system, but at the expense of design complexity [7]. This system obtained a jump height of 20 cm, but perhaps as a testament to the challenge of this approach, left for future work a spring reload system, and its jump variability was limited to the upper of the range 35%. Its design is therefore unable to perform small jumps that might be needed to reach a precise location. In biology, work multiplication is not observed at all. A possible explanation could be that an extremely high jump is just not that evolutionarily valuable relative to the cost in complexity, and that it is sufficient if common obstacles can be surmounted. For example, a stair step in an urban setting.

Here we introduce a directly-actuated design that represents a fundamental departure from such "store-and-release" mechanisms. We show that engineered electromagnetic actuators—low-inertia coreless DC motors operating well above their thermal limit for a short period of time—can achieve instantaneous power density large enough to obtain a jump height high enough for practical application. More

*This work was partly supported by the NSF awards 2319060, 2054850, and 2235207.

[1]Department of Mechanical Engineering, [2]Paul G. Allen School of Computer Science, University of Washington, Seattle, WA 98195, USA. hw328@uw.edu

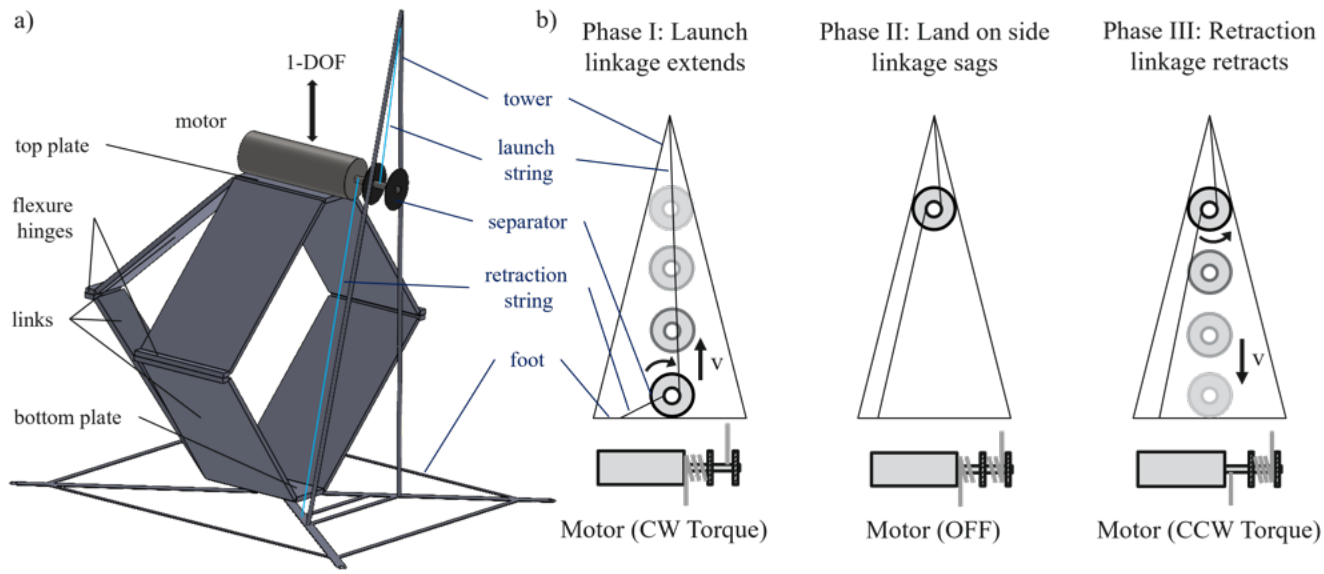

Fig. 2. **Working principle of the direct-drive mechanism.** (a) The 3D folding motion of the sarrus linkage is kinematically equivalent to a simple 1-DOF prismatic joint, constraining motion to purely vertical translation. The top plate is bonded to the motor and the bottom plate is bonded to the foot. The roll cage is omitted for presentation simplicity. (b) Schematic 2D views of the three operational phases shown with respect to the body frame. The front view (top) shows the translational motion of the motor and pulley (middle circle). A side view (bottom) shows the spooling state of the two strings. During Launch (I), clockwise rotation tensions the launch string to lift the robot, while the retraction string unspools. Post-landing (II), the linkage is in an extended state with the robot in one of the parasitic stable equilibria. During Retraction (III), counter-clockwise rotation tensions the retraction string to pull the motor back into proximity with the foot for self-righting. To avoid tangling and keep the two strings separate, two rigid carbon fiber spooling separator flanges are press-fit onto the motor shaft.

importantly, by coupling the motor directly to the propulsive limb, we recover full closed-loop authority throughout both the jump and retraction process. The torque of the motor is directly proportional to current in its windings. In a direct-drive linkage, this torque maps linearly to the ground reaction force. This architectural change enables the robot to actively modulate thrust to achieve variable hop heights. Another example of agile locomotion capability that exemplifies the advantage of this approach is the four-legged direct-drive MIT Cheetah [8]. Direct-drive hoppers have remained largely unexplored at the sub-gram scale, however.

This paper presents the design, fabrication, and control of a near sub-gram, direct-drive hopping robot that challenges the conventional wisdom of impulsive microrobotics. The specific contributions of this work are:

- A microfabricated direct-drive jumping mechanism design capable of surmounting a key obstacle: a standard stair step (17 cm high). The jumping mechanism does not use springs or latches, simplifying its design.
- Experimental confirmation of a linear relationship between commanded current and jump height, validating the predictability of the direct-drive approach.
- An active retraction system driven by the primary actuator that self-rights the robot that enables autonomous, repeatable multi-jump missions.
- A characterization of the system efficiency.

II. System Design and Fabrication

To maximize jump height, the moving mass must be maximized, while the foot mass must be minimized. Because of the small scale, physical structure makes up a small fraction of total mass (<20%), so the cage is attached to the foot. The remainder, consisting of the actuator, and, in the future, battery and autonomy payload, constitutes the mass that is accelerated upward.

A. Actuator Selection

We selected the actuator to ensure it could surmount the primary anticipated obstacle to free motion: a standard (17 cm) stair step. This provided a lower bound on power density. Other considerations included efficiency and simplicity of the drive electronics. Piezoelectric cantilever or stacked actuators, while precise, have a limited stroke length ($\sim 100\,\mu\text{m}$), necessitating a complex transmission, and requiring complex high-voltage electronics. Shape Memory Alloys (SMAs) offer high energy density but low efficiency, and lack the bandwidth required for direct actuation due to slow thermal time constants [9].

We selected a low-cost ($2) sub-gram, coreless DC motor ($4\,\text{mm}$ diameter, $7\,\Omega$ coil resistance, $820\,\text{mg}$, Micron Wings, Australia) for the direct-drive configuration. Unlike larger iron-core motors, coreless rotors minimize rotational inertia, enabling the rapid acceleration required for impulsive jumping.

B. Linearly Constrained Transmission

To convert the rotary output of the DC motor into translational motion, we used a lightweight spooling mechanism. Two high-toughness polyethylene fishing lines (Berkley Fireline, 3 kg test) were bonded to the motor shaft using cyanoacrylate (CA). The other end of the first was bonded to a carbon fiber support tower constructed from two rods

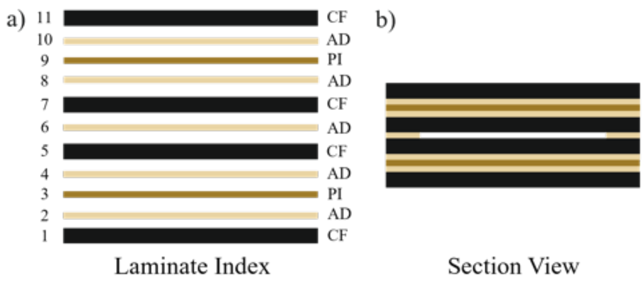

Fig. 3. **Sarrus linkage layup.** (a) Layup layers and (b) stacked cross-sectional view for the sarrus linkage fabrication. Materials are 122 µm $0° - 90° - 0° - 90°$ carbon fiber laminate (Toho Tenax Q-1112 0300, 27 grams/m^2) (CF), 13 µm American Durafilm polyimide film (PI), and DuPont FR1500 Pyralux sheet adhesive (AD).

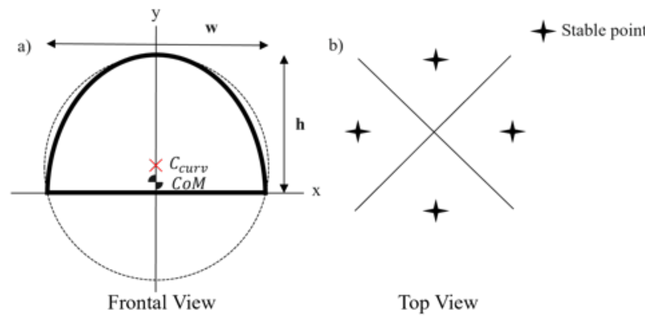

Fig. 4. **Geometric stability analysis of the self-righting roll cage.** (a) Frontal projection illustrating the sufficient condition for monostability. The circular shape (thin line) approximates a truncated ellipsoid of the cage (thick line). The aspect ratio, $R = h/w$, is optimized for passive self-righting. (b) Top-down view of the 3D cage formed by two orthogonal 2D profiles. The four star markers indicate the parasitic stable equilibria located at the inter-cardinal points that occur when the sarrus linkage is extended, that is, at the end of a jump, before the motor has been retracted.

in a rigid triangle. The second, used in the retraction mechanism, was fixed to the foot (Fig. 2). Two circular laser-machined separators were press-fit onto the motor axle to keep the string in place in its spool and avoid tangling. To maximize the transfer of mechanical work from the motor into robot kinetic energy, we constructed a sarrus linkage with $40\,\mathrm{mm}$ of translational travel between the foot and the payload. The sarrus linkage constrains motion to be linear (prismatic), ensuring that the force from the string, which applies at a distance from the motor's center of mass, does not apply a torque to the system in addition to the jumping force. To construct the sarrus linkage, we used the Smart Composite Microstructures (SCM) process [10], [11], using a 355 nm diode-pumped solid state laser (Photomachining, Inc., Pelham, NH), prepreg carbon fiber composites, and pin-aligned thermal sheet adhesion with 11 total layers (Fig. 3).

C. Self-Righting Architecture

To enable multi-jumping, the robot must reliably right itself back onto its foot from unpredictable landing orientations. The direct-drive nature of our design, in addition to allowing jump height modulation, simplifies self-righting. Motor retraction can be controlled, allowing for either small perturbations if the robot is stuck in an undesired orientation, and facilitates positioning the motor close to the foot to lower the system center of mass (CoM).

We designed the enclosing cage to passively right the robot when its CoM is near the foot [12], [13]. However, when retracted, our sarrus linkage extends outside of the bounds of the cage. To overcome the resulting local stable equilibria, we employed a dynamic approach, rapidly retracting the motor, which almost always rights the robot onto its foot.

1) Geometric Optimization of the Passive Hull: The attitude recovery system is a passive carbon fiber roll cage inspired by tortoise shell morphology. The geometry condition for passive self-righting requires that the system's CoM remains strictly below the hull's local center of curvature (C_{curv}) at all ground contact points. We utilized the geometric framework proposed by Domokos et al. [12], which found that a height-to-width aspect ratio of $R \approx 0.9$ maximizes monostatic stability for homogeneous shells (Fig. 4a).

The cage was fabricated by machining the foot to the desired width using carbon fiber composite for rigidity, and scaling it by R to determine the height, using flexible carbon fiber rods ($0.25\,\mathrm{mm}$ diameter, Micron Wings, Australia) to form the shape. The structure consists of two orthogonal 2D profiles intersecting at the central vertical axis, anchored to the foot with cyanoacrylate adhesive and bonded at the top intersection. While the idealized 2D profile exhibits purely monostatic behavior, when the sarrus linkage is extended, the 3D structure has four parasitic stable equilibria located at the inter-cardinal points between the carbon fiber ribs (Fig. 4b).

2) Active CoM Modulation and Dynamic Perturbation: Because the $820\,\mathrm{mg}$ motor accounts for over 80% of the total system mass, it acts as the functional CoM. During Phase II (Fig. 2b), the motor sits elevated within the cage, violating the righting condition (CoM below C_{curv}). To bring the motor into proximity with the foot and self-right, the motor direction is reversed by reversing polarity. The motor spools in the counter-clockwise direction, tensioning the retraction string (Fig. 2b).

Active retraction achieves self-righting through two coupled physical mechanisms. First, by physically hauling the heavy motor back to the foot, the system actively forces the CoM back below the center of curvature (C_{curv}), satisfying the geometric requirements of the passive hull. Second, the rapid downward acceleration of the motor mass creates a dynamic momentum transfer that forcefully kicks the robot out of the shallow local energy wells of the 3D cage, initiating the gravitational torque readjusting the robot's orientation. Self-righting process thus occurs in three steps:

1) **impact and passive reorientation:** The cage elastically deforms to reduce impact shock, then rolls into a stable configuration away from the foot.
2) **active CoM shift:** The motor counter-spools the retraction string and moves the center of mass to be below the center of curvature.
3) **gravitational restoration:** Once the center of mass crosses the critical stability boundary, gravitational torque passively rotates the robot into its upright position without further actuation. This is a dynamic process, so the robot undergoes a short airborne phase.

III. Control Architecture

Future work will implement onboard power and control. Before that is ready, we needed a power tether to do system design and characterization. To do so, thin wires are needed to minimize the effect on the robot's jump and self-righting, but this adds a serial resistance of comparable magnitude to the motor windings themselves. Serial resistance itself is not a problem if its value is known. The challenge is that changes to the wire conformation or length, such as when it breaks and a replacement is needed, can have a large effect on the torque produced by the motor because of the voltage drop across the wires. To minimize this effect, we designed a feedback-controlled current control system, rather than voltage control. Current control ensures that the motor delivers constant torque regardless of the robot's speed or the battery voltage, effectively rejecting the effect of uncertain serial resistance, and back-EMF disturbance. In future work when this tether is no longer needed and power is supplied onboard, we anticipate converting to a simpler pulse-width-modulated (PWM) voltage controller.

The current controller relies on an off-board power supply and a digital control unit. A DC power supply provides $8.0\,\mathrm{V}$ to ensure that adequate voltage is available to mitigate the voltage drop across the tethered power wires. We used a dual H-bridge motor driver (TI DRV8833) via pulse width modulation (PWM) at $40\,\mathrm{kHz}$. An H-bridge allows bidirectional control, so that the robot can both jump and retract. Motor current was sensed using a hall-effect current sensor (Allegro ACS724, Pololu Robotics, Las Vegas NV USA.). We used an Arduino UNO R1 board to measure this signal using its analog to digital converter, and ran the control loop at $1\,\mathrm{kHz}$. The signal from the current sensor was conditioned using a digital low-pass exponential moving average (EMA) filter [14] ($\alpha = 0.1$) to reduce high-frequency switching noise. The control structure consisted of a parallel feedforward-feedback loop (Fig. 5).

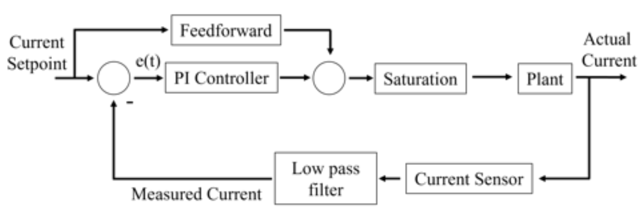

Fig. 5. **Block Diagram of the motor current control system.** The feedforward term provides the baseline voltage to compensate for the expected voltage drop due to the serial resistance of the thin tether wiring, while the PI controller compensates for disturbances and dynamic errors. The output was clamped to protect overvoltage and burnout of the $4.2\,\mathrm{V}$ motor coil from the $8\,\mathrm{V}$ supply.

We used a proportional-integral (PI) controller to correct for model uncertainties, small disturbances, and resistance change due to heating. Relying solely on a PI controller introduces a delay, however, because an error must exist before the controller reacts. In a jumping scenario, where the launch phase lasts only milliseconds, this delay represents a significant drawback. To overcome this, we applied a feedforward control term (K_{ff}) as shown in Fig. 5. Using Ohm's law, the required average voltage is the product of the target current and the motor's terminal resistance (R_{coil}). By dividing this required voltage by the nominal supply voltage (V_{nom}), we obtain the necessary duty cycle:

$$K_{\mathrm{ff}} = \left(\frac{R_{\mathrm{coil}} \cdot I_{\mathrm{set}}}{V_{\mathrm{nom}}} \right). \tag{1}$$

This term represents the baseline PWM duty cycle required to sustain the target steady-state current (I_{set}).

IV. Results

A. Current Controller

To validate our current control system, we first characterized its current output step response in closed loop when connected to the actuator. The primary objective of the controller is to reach the target current setpoint with minimal rise time and overshoot. We placed the robot on its foot in the launch position on a flat tabletop with the tether power wire suspended in a higher platform to minimize force and torque from the tether. We evaluated the transient response of the motor current controller during jumps by measuring its rise time (from 10% to 90% of the steady-state) and percent overshoot. These metrics were calculated for each of the five experimental trials across all three setpoints. We hand-tuned the three control parameters, K_{p}, K_{i}, and K_{ff} to maximize this objective. At high frequencies, the "on-resistance" of the H-bridge effectively increases because its MOSFET transistors spend a significant amount of time in the transition phase. This reduces the voltage reaching the motor; therefore, we increased the baseline feedforward term K_{ff} by approximately 25%.

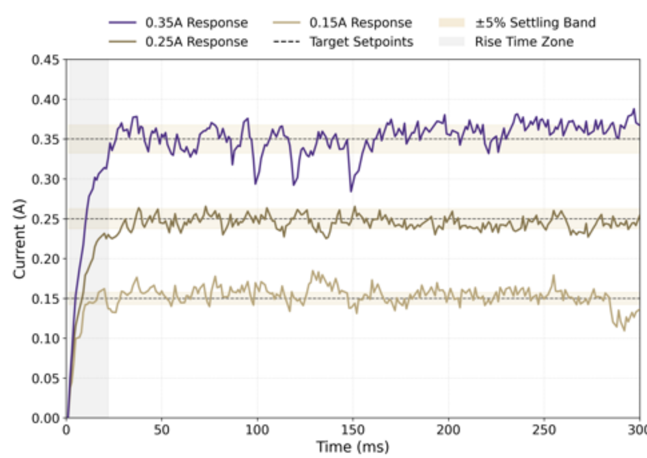

Fig. 6. Step response of the motor controller for three different current setpoints. Dashed black lines indicate the commanded setpoints.

Fig. 6 shows electrical current step responses for three different setpoints after tuning. We were able to obtain an average rise time of approximately $20\,\mathrm{ms}$, less than $20\,\%$ overshoot, and steady-state error below $5\,\%$ of the current setpoint. We observe that the $0.15\,\mathrm{A}$ setpoint has a higher average overshoot, which may be attributable to the low signal-to-noise ratio of the ACS724 current sensor at low current magnitude.

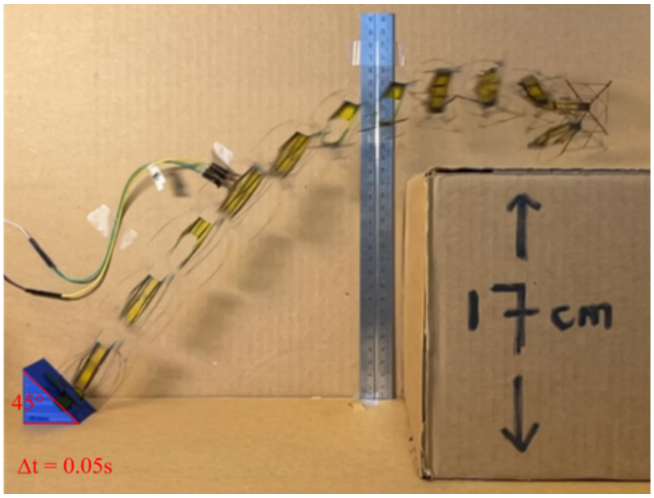

Fig. 7. **Stroboscopic sequence of a representative stair-surmounting jump taken from a single 240 FPS recording, with frames extracted at** $0.05\,\mathrm{s}$ **intervals.** By placing onto a 45° ramp, the direct-drive mechanism achieves the forward trajectory to clear a $17\,\mathrm{cm}$ obstacle, simulating a standard stair. Operating at $0.35\,\mathrm{A}$, frames track from liftoff through apex.

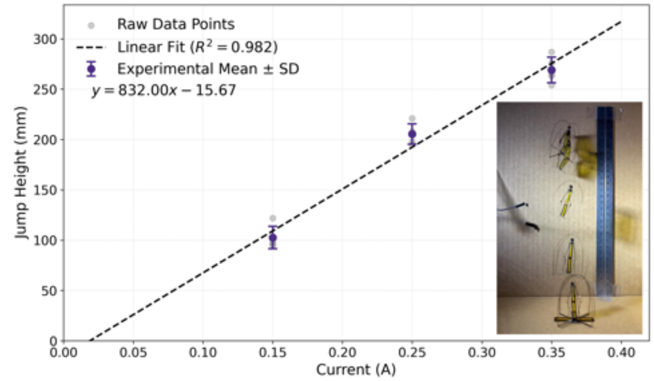

Fig. 8. **Measured** CoM **jump height versus input current setpoint shows a near-linear relationship.** Individual trial results are shown as semi-transparent grey markers (one $0.35\,\mathrm{A}$ setpoint jump is shown) to illustrate experimental variance. The purple markers and error bars represent the mean and standard deviation (n = 5 for each current setpoint). The dashed line indicates the linear regression fit ($R \approx 0.98$).

Our experimental results validated the use of an $8\,\mathrm{V}$ supply to drive the nominal $4.2\,\mathrm{V}$ actuator as a method to ensure high-bandwidth current control. Rather than serving as a simple power boost, this voltage overhead provides the necessary control range to effectively bypass the electrical time constant of the motor. By providing a voltage significantly higher than the nominal rating, the controller maintains the authority required to command precise current setpoints despite the inductive lag and back-electromotive force inherent in the system.

The feedforward term K_{ff} proved critical for maintaining stability during these high-speed transitions. As evidenced in the transient response plots, the current transitions smoothly from the acceleration phase to the steady-state phase. The minimal overshoot confirms that the system is well-damped. This is important for direct-drive jumping, as excessive current overshoot could briefly exceed the thermal or magnetic saturation limits of the coreless motor, leading to permanent damage or non-linear torque saturation.

B. Jumping Performance

We measured jump height using a slow-motion mobile phone camera and a ruler. The launch phase before the foot leaves the ground takes approximately $15\,\mathrm{ms}$. Fig. 8 shows that there is a linear correlation ($R^2 \approx 0.98$) between coil current setpoint and the maximum jump height. This linearity is a characteristic of the direct-drive force mechanism, where force is directly proportional to the current [15]. This contrasts with spring-loaded systems, in which energy release is often variable and non-linear due to cam profiles and latch friction [16]. This deterministic relationship simplifies the high-level planning problem, allowing the robot to more accurately specify specific jump heights to clear obstacles of known dimensions. We validated the proposed $17\,\mathrm{cm}$ stair surmounting in Fig. 7. We additionally showed that by adding a pair of small (1 cm) feet to tilt the robot, and driving it at a very low level, it could perform very short (<5 mm) jumps for precise positioning (Supplementary Video).

C. Self-Righting Performance

While ascent trajectories remain highly repeatable, post-landing behavior exhibits more variability due to surface interactions and impact restitution. To achieve multi-jump autonomy despite this unpredictability, the system must self-right onto a foot that provides a consistent orientation in space. It does so as described above by reversing the motor to retract it into contact with the foot. This active bidirectional authority enables rapid, sequential operations.

To quantify the self-righting capability independent of the tether, which can slightly alter the robot's rotational dynamics, we conducted isolated self-righting tests. The robot was manually positioned into one of the stable equilibria as shown in Fig. 4b when the sarrus linkage was extended in the post-landing posture. In this phase, the launch string is taut and the retraction string is slack. We then commanded the motor to retract to bring it in contact with the foot to lower its CoM and destabilize the local minima. A representative self-righting sequence (is detailed in Fig. 9) shows how this process almost always restores the robot to its upright launch configuration.

The robot achieved a 90% righting success rate on a flat and rigid surface across 10 trials. The average recovery time from a worst-case inverted landing to a ready-to-jump configuration was $4\,\mathrm{s}$. These results experimentally validated that combining a turtle-inspired passive cage with active CoM modulation enables reliable autonomous recovery across repeated jump cycles for continuous jumping tasks.

Finally, to demonstrate continuous multi-jump capability, we successfully executed a sequence of four consecutive jumps at the $0.35\,\mathrm{A}$ setpoint (Supplementary Video). We stopped jumping only because tangling in the power tether wires began to impede performance.

V. Discussion

A. Comparative Analysis

To contextualize the performance of the proposed direct-drive system, we compare it against some existing state-of-

TABLE I
PERFORMANCE COMPARISON OF SMALL-SCALE SUB-10G JUMPING ROBOTS.

Platform	Mass (g)	Jump Height (cm)	Jump Height (body lengths)	**Self-Righting**	**Height Modulation**	Power
MIT Hybrid Hopper [17]	∼1	20	5	No	Yes	Tethered
This Work	**1.0**	**28**	**5**	**Yes**	**Yes**	**Tethered**
SNU Flea-inspired [5]	1.1	64	30	No	No	Tethered
HAMR [4]	2.2	140	23	Yes	No	Tethered
Click Beetle-inspired [18]	2.6	95	29	No	No	Auton.
Tribot [19]	4.0	22	5	No	No	Tethered
EPFL Jumper [13]	9.8	76	6	Yes	Yes	Auton.

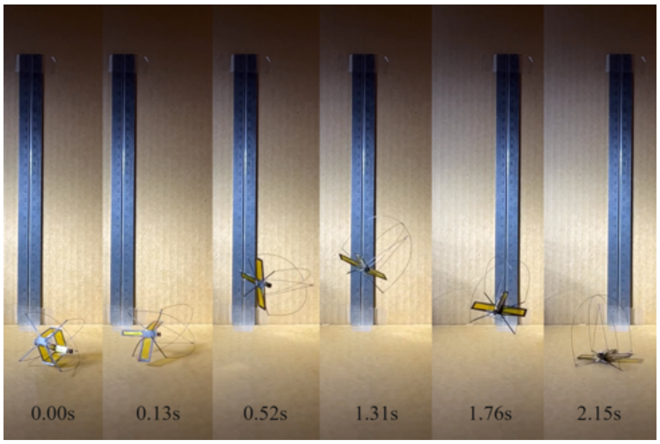

Fig. 9. **Self-righting sequence extracted from a video of a representative jump.** At 0.00 s, the system has completed step 1: impact and passive orientation, arriving at a stable equilibrium. At 0.13 s, the robot begins step 2: active CoM shift, by retracting the motor toward the foot. This dynamic motion induces a brief airborne phase during self-righting. By the end of the sequence, the motor has moved into contact with the foot. In step 3: gravitational restoration, the CoM is now low enough that the system usually lands on its foot. Self-righting takes about 2 s to complete.

the-art small-scale jumping robots in Table I. Existing platforms predominantly utilize Latch-Mediated Spring Actuation (LaMSA) to overcome the power density limits of small actuators. While platforms such as the piezo-driven HAMR [4] and SMA-driven flea robots [5] achieve impressive jump heights exceeding 20 body lengths, this performance comes at the cost of control authority. The snap-through instability used to release energy is inherently binary, preventing intermediate height adjustments. Furthermore, many high-power jumpers lack integrated self-righting mechanisms, rendering them single-shot devices in unstructured terrain.

In contrast, our direct-drive architecture occupies a unique design space. As shown in Table I, it is the only near sub-1g platform capable of both active self-righting and modulating height. While our peak CoM jump height (28.6 cm) is lower than purely ballistic spring-loaded systems, our direct-drive architecture allows the robot to precisely dial in partial jumps for efficient navigation in cluttered environments, eliminating the mechanical complexity required by variable-latch mechanisms. This trade-off between raw ballistic power and continuous control authority prioritizes repeatable, targeted mobility over single-event peak performance.

B. Jump Efficiency

Efficiency is defined as the ratio of useful potential energy gained to the total electrical energy consumed during the launch phase. This metric represents a theoretical upper bound, as it neglects aerodynamic drag and mechanical losses such as flexure hysteresis and friction:

$$\eta = \frac{E_{\text{mech}}}{E_{\text{elec}}} = \frac{E_{\text{mech}}}{E_{\text{mech}} + E_{\text{diss,launch}}}, \quad (2)$$

where $E_{\text{mech}} = mg\bar{h}$ represents the change in gravitational potential energy, and $E_{\text{diss,launch}}$ represents the resistive Joule heating losses in the coil for the jump.

With a $\bar{h} = 269\,\text{mm}$ (the mean CoM jump height at a setpoint of $0.35\,\text{A}$ from the five data points in Fig. 8) and a total robot mass of $m = 1.0\,\text{g}$, the useful mechanical work is $E_{\text{mech}} \approx 2.69\,\text{mJ}$. The resistive losses were calculated by numerically integrating current measurements (Fig. 6) over the $T_{\text{launch}} = 15\,\text{ms}$ duration:

$$E_{\text{diss,launch}} = \int_0^{T_{\text{launch}}} i(t)^2 R \; dt \approx 4.29\,\text{mJ}, \quad (3)$$

assuming a nominal motor resistance of $R = 7.0\,\Omega$. This gives a jump efficiency of $\eta \approx 39.0\%$. The retraction phase takes significantly less force, so we assume its mechanical power is negligible. For the duration $T_{\text{retract}} \approx 13\,\text{ms}$ the energy dissipation is estimated to be $E_{\text{diss,retract}} \approx 2.56\,\text{mJ}$.

Jump efficiency is lower than transmission-based systems [20], but this can be attributed primarily to lower efficiency in small motors (40–50% at this size). Assuming equality of kinetic and potential energy, the liftoff speed is approximately $v_0 = \sqrt{2g\bar{h}} = 2.3\,\text{m}\,\text{s}^{-1}$. The motor angular velocity at this point is $n = \frac{60 v_0}{2\pi r} = 44{,}000$ rotations/minute (RPM) for the $r = 0.5\,\text{mm}$ motor axle radius. This motor's free-spinning rotation rate is $n_o \approx 60,000$ RPM at 2.45 V. Hence, the relatively high efficiency can be attributed to good impedance matching of the system, operating the motor close its peak efficiency and power levels near $n_0/2$ RPM.

C. Locomotion Efficiency

To estimate a theoretical lower bound for our mass-specific Cost of Transport (CoT), we assume the kinetic energy generated during a mean CoM jump at the $0.35\,\text{A}$ operating current ($\bar{h} = 0.269\,\text{m}$) is redirected into an optimal 45° ballistic trajectory. It should be noted that this is a hypothetical projection based on vertical performance, and real-world CoT would be higher due to unmodeled losses and imperfect energy redirection. This projection gives a mean horizontal distance per jump of $\bar{d} = 0.538\,\text{m}$. Given the total energy consumption of $E_{\text{tot}} \approx 9.54\,\text{mJ}$ ($4.29\,\text{mJ}$ (launch) and $2.56\,\text{mJ}$ (retract) for energy dissipation in the coil and

$2.69\,\mathrm{mJ}$ for actual work of the jump), and a system mass $m = 1.0\,\mathrm{g}$, the mass-specific CoT for the DirectHop is:

$$CoT = \frac{E_{\mathrm{tot}}}{m\bar{d}} \approx 18\,\mathrm{J\,kg^{-1}\,m^{-1}}. \quad (4)$$

The CoT of DirectHop compares well to other systems that are similarly capable of surmounting urban obstacles. For comparison, the $80\,\mathrm{mg}$ flying insect robot presented in [21] has a CoT of approximately $0.08\,\mathrm{J\,m^{-1}}$ after 25% efficient boost converter factored in, for a mass-specific CoT of approximately $1000\,\mathrm{J\,kg^{-1}\,m^{-1}}$. Recent hybrid platforms, such as the MIT sub-gram hybrid hopper [17], improve efficiency by incorporating elastic storage element to recover impact energy into a flying chassis. This multi-modal approach reduces CoT by a factor of approximately $2\times$ relative to pure flight. While hopping flight can increase payload capacity and reduce CoT, and provides for rapid locomotion, energy usage remains on the order of $100\times$ larger than our hopper. This metric highlights a fundamental advantage of impulsive jumping over sustained flight at the microrobot scale. Finally, while this low CoT provides a promising pathway toward power autonomy, sustaining the high instantaneous current required for direct-drive actuation remains an open challenge; future battery and energy harvesting operations will likely require hybrid power architectures (see below).

D. Actuator Power Density vs. Biological Muscle

To contextualize the performance of the direct-drive architecture, we compare the mechanical power density of the coreless DC motor to that of biological muscle. In jumping insects, the muscle is limited to a direct contraction power density of approximately $100\,\mathrm{W\,kg^{-1}}$ [22].

The engineered electromagnetic actuator is subject to different constraints than biological tissue. Over the $15\,\mathrm{ms}$ launch window, the DC motor generates $2.69\,\mathrm{mJ}$ of useful mechanical work. This equates to an average mechanical power output of:

$$P_{\mathrm{avg}} = \frac{E_{\mathrm{mech}}}{T_{\mathrm{launch}}} = \frac{0.002\,69\,\mathrm{J}}{0.015\,\mathrm{s}} \approx 0.179\,\mathrm{W}. \quad (5)$$

Given the motor's isolated mass of $m_{\mathrm{motor}} = 820\,\mathrm{mg}$, the mass-specific mechanical power density is:

$$\rho_{\mathrm{power}} = \frac{P_{\mathrm{avg}}}{m_{\mathrm{motor}}} = \frac{0.179\,\mathrm{W}}{0.000\,82\,\mathrm{kg}} \approx 218\,\mathrm{W\,kg^{-1}}. \quad (6)$$

This represents a mechanical power density of the sub-gram motor that is more than double the theoretical limit of direct biological muscle contraction. This allows our system to operate without mechanical energy storage.

E. Battery- and Solar-powered Operation

Here we consider whether a battery or solar photovoltaics can provide sufficient voltage and power for our system. In the tethered configuration, the system operated at $8\,\mathrm{V}$ to ensure enough voltage headroom to against series resistance and the motor's back-EMF voltage. However, achieving the requried saturation current at the onset of a jump demands:

$$V_{\mathrm{min}} = I_{\mathrm{set}} R_{\mathrm{coil}} = (0.35\,\mathrm{A})(7\,\Omega) \approx 2.45\,\mathrm{V}. \quad (7)$$

Batteries are also constrained by power they can produce per unit mass (power density). If we consider average power during the period of motor actuation, off-the-shelf lithium-polymer battery chemistry is sufficient. During the $15\,\mathrm{ms}$ extension period, the battery must supply $E_{\mathrm{elec}} = 6.98\,\mathrm{mJ}$, for an average power of $465\,\mathrm{mW}$. The $330\,\mathrm{mg}$ $8\,\mathrm{mA\,h}$ GM300910 battery (Powerstream, Inc.) can supply up to 120 mA at 3.5 V (420 mW), for a power density of 1.3 W/g. Scaling this up to a 500 mg battery would provide enough power in this scenario. At about 100 J, such a battery could power on the order of 10,000 jumps. It is a bit more challenging to power the system if we consider instantaneous rather than average power. Dissipation goes up to 540 mW ($P = i^2R$, while $i = 0.28\,\mathrm{A}$ at $15\,\mathrm{ms}$) as current develops in the coils, and mechanical power increases with time as the system accelerates upward. We anticipate that a combination of two approaches can reduce instantaneous power needs. First, we could apply a sudden transient to the feedforward signal so that the current remains relatively constant, rather than increasing with time. Second, small 100μF capacitors, each weighing approximately 7.5 mg and storing up to $E = \frac{1}{2}CV^2 = 0.8$ mJ [23], could supply some of the transient load without significant added weight.

Adding a $500\,\mathrm{mg}$ battery and a $100\,\mathrm{mg}$ control/power board (e.g. [24]) reduces expected jump height. Assuming the actuator generates a constant mechanical power output during the stroke, jump height for the autonomous system h_{auto} scales by the mass ratio:

$$h_{\mathrm{auto}} = \bar{h}\left(\frac{m}{m_{\mathrm{auto}}}\right) = 269\,\mathrm{mm}\left(\frac{1.0}{1.62}\right) \approx 166\,\mathrm{mm}. \quad (8)$$

With feedforward optimizations to shorten the current rise time, this projected height still approaches the clearance needed for a standard $17\,\mathrm{cm}$ stair step.

A rough order of magnitude estimate shows the potential for solar operation. A high-efficiency photovoltaic array in full sun produces up to 1 mW/mg (MicroLink Devices, Inc., Chicago IL). If a jump consumes 10 mJ, then a 10 mg array (negligible mass and $0.5\,\mathrm{cm^2}$ area) would power one jump approximately every second. Even in indoor lighting (approximately $100\times$ weaker) expanding the array to 100 mg ($5\,\mathrm{cm^2}$) would power a jump every ten seconds. In this scenario, instantaneous power could be provided entirely from capacitors [23], [25], lowering overall system weight relative to battery-powered operation.

VI. Conclusions

This work introduces a directly-actuated 1.0 g jumper inspired by the continuous control paradigm of larger biological organisms. By utilizing a motor and pulley in direct drive, we avoid the mechanical complexity of springs and latches while retaining the ability to surmount a standard stair step. Experimental results confirm a linear relationship between input current and jump height, allowing for predictable jump heights. We also demonstrated that a very weak input could produce short (<5 mm) forward jumps with a tilted foot for more precise position control. A predictability that enables precise locomotion for applications such as urban mobility and targeted sensor deployment. The resulting system achieves a Cost of Transport nearly two orders of magnitude lower than sustained flight, highlighting direct-drive jumping as a highly efficient alternative for obstacle traversal at this scale.

Multi-jump autonomy is enabled by a passive, tortoise-inspired roll cage and an active retraction mechanism that achieved a 90% self-righting success rate. This architecture was made possible by Smart Composite Microstructures (SCM) [10], [11], which provided high-strength, low-weight kinematic linkages comprising only 20% of the total mass. Furthermore, high-precision laser microfabrication allowed for integrated foot alignment features that prevent string tangling during high-speed spooling.

Operating at the sub-gram scale offers distinct advantages. Favorable surface-area-to-volume scaling enhances the viability of energy harvesting [26], [25], with our results suggesting a jump rate of once per second is feasible under direct sunlight. The design is also highly cost-effective, with the motor and structural materials totaling just a few dollars.

Future work will focus on increasing jump height via optimized motor windings and feedforward control to shorten rise time. We also plan to introduce a tilted foot for forward locomotion and a $300\,\mathrm{mg}$ vibration motor for directional steering. Finally, we will explore hybrid power architectures to sustainably manage the high instantaneous current demands of direct-drive actuation, and add an onboard control system.

ACKNOWLEDGMENT

The authors would like to thank Arjun Subramanian for inspiration in the design phase.

REFERENCES

[1] E. W. Hawkes, C. Xiao, R.-A. Peloquin, C. Keeley, M. R. Begley, M. T. Pope, and G. Niemeyer, "Engineered jumpers overcome biological limits via work multiplication," *Nature*, vol. 604, pp. 657–661, Apr. 2022.

[2] H. C. Bennet-Clark and E. C. A. Lucey, "The Jump of the Flea: A Study of the Energetics and a Model of the Mechanism," *Journal of Experimental Biology*, vol. 47, pp. 59–76, Aug. 1967.

[3] M. Burrows, "Jumping performance of froghopper insects," *Journal of Experimental Biology*, vol. 209, pp. 4607–4621, Dec. 2006.

[4] F. Ramirez Serrano, N.-s. P. Hyun, E. Steinhardt, P.-L. Lechère, and R. J. Wood, "A springtail-inspired multimodal walking-jumping microrobot," *Science Robotics*, vol. 10, p. eadp7854, Feb. 2025.

[5] M. Noh, S.-W. Kim, S. An, J.-S. Koh, and K.-J. Cho, "Flea-Inspired Catapult Mechanism for Miniature Jumping Robots," *IEEE Transactions on Robotics*, vol. 28, pp. 1007–1018, Oct. 2012.

[6] V. Zaitsev, O. Gvirsman, U. Ben Hanan, A. Weiss, A. Ayali, and G. Kosa, "A locust-inspired miniature jumping robot," *Bioinspiration & Biomimetics*, vol. 10, p. 066012, Nov. 2015.

[7] S. Divi, R. St. Pierre, H. M. Foong, and S. Bergbreiter, "Controlling jumps through latches in small jumping robots," *Bioinspiration & Biomimetics*, vol. 18, no. 6, p. 066003, 2023.

[8] G. Bledt, M. J. Powell, B. Katz, J. Di Carlo, P. M. Wensing, and S. Kim, "MIT Cheetah 3: Design and Control of a Robust, Dynamic Quadruped Robot," in *2018 IEEE/RSJ International Conference on Intelligent Robots and Systems (IROS)*, pp. 2245–2252, Oct. 2018. ISSN: 2153-0866.

[9] Y. Tadesse, N. Thayer, and S. Priya, "Tailoring the Response Time of Shape Memory Alloy Wires through Active Cooling and Pre-stress," *Journal of Intelligent Material Systems and Structures*, vol. 21, pp. 19–40, Jan. 2010.

[10] R. J. Wood, "The First Takeoff of a Biologically Inspired At-Scale Robotic Insect," *IEEE Transactions on Robotics*, vol. 24, pp. 341–347, Apr. 2008.

[11] J. P. Whitney, P. S. Sreetharan, K. Y. Ma, and R. J. Wood, "Pop-up book MEMS," *Journal of Micromechanics and Microengineering*, vol. 21, p. 115021, Oct. 2011.

[12] G. Domokos and P. L. Várkonyi, "Geometry and self-righting of turtles," *Proceedings of the Royal Society B: Biological Sciences*, vol. 275, pp. 11–17, Oct. 2007.

[13] M. Kovač, M. Schlegel, J.-C. Zufferey, and D. Floreano, "A miniature jumping robot with self-recovery capabilities," in *2009 IEEE/RSJ International Conference on Intelligent Robots and Systems*, pp. 583–588, Oct. 2009.

[14] M. Fikri, S. Herdjunanto, and A. Cahyadi, "On the Performance Similarity Between Exponential Moving Average and Discrete Linear Kalman Filter," in *2019 Asia Pacific Conference on Research in Industrial and Systems Engineering (APCoRISE)*, pp. 1–5, Apr. 2019.

[15] P. M. Wensing, A. Wang, S. Seok, D. Otten, J. Lang, and S. Kim, "Proprioceptive Actuator Design in the MIT Cheetah: Impact Mitigation and High-Bandwidth Physical Interaction for Dynamic Legged Robots," *IEEE Transactions on Robotics*, vol. 33, pp. 509–522, June 2017.

[16] M. Ilton, M. S. Bhamla, X. Ma, S. M. Cox, L. L. Fitchett, Y. Kim, J.-s. Koh, D. Krishnamurthy, C.-Y. Kuo, F. Z. Temel, A. J. Crosby, M. Prakash, G. P. Sutton, R. J. Wood, E. Azizi, S. Bergbreiter, and S. N. Patek, "The principles of cascading power limits in small, fast biological and engineered systems," *Science*, vol. 360, p. eaao1082, Apr. 2018.

[17] Y.-H. Hsiao, S. Bai, Z. Guan, S. Kim, Z. Ren, P. Chirarattananon, and Y. Chen, "Hybrid locomotion at the insect scale: Combined flying and jumping for enhanced efficiency and versatility," *Science Advances*, vol. 11, p. eadu4474, Apr. 2025.

[18] L. Cao, G. Lu, Z. Wang, B. Peng, J. Wu, S. Gorb, and Y. Wu, "A 2.6-g Untethered Microrobot with Maneuverable Crawling and High Jumping Performance," *Soft Robotics*, p. 21695172251394586, Nov. 2025.

[19] Z. Zhakypov, C. H. Belke, and J. Paik, "Tribot: A deployable, self-righting and multi-locomotive origami robot," in *2017 IEEE/RSJ International Conference on Intelligent Robots and Systems (IROS)*, pp. 5580–5586, Sept. 2017. ISSN: 2153-0866.

[20] S. Seok, A. Wang, M. Y. Chuah, D. J. Hyun, J. Lee, D. M. Otten, J. H. Lang, and S. Kim, "Design Principles for Energy-Efficient Legged Locomotion and Implementation on the MIT Cheetah Robot," *IEEE/ASME Transactions on Mechatronics*, vol. 20, pp. 1117–1129, June 2015.

[21] Y. M. Chukewad, J. James, A. Singh, and S. Fuller, "RoboFly: An Insect-Sized Robot With Simplified Fabrication That Is Capable of Flight, Ground, and Water Surface Locomotion," *IEEE Transactions on Robotics*, vol. 37, pp. 2025–2040, Dec. 2021.

[22] C. K. Goode, C. Woodrow, S. L. Harrison, D. C. Deeming, and G. P. Sutton, "Control of high-speed jumps in muscle and spring actuated systems: a comparative study of take-off energetics in bush-crickets (Mecopoda elongata) and locusts (Schistocerca gregaria)," *Journal of Comparative Physiology. B, Biochemical, Systemic, and Environmental Physiology*, vol. 193, no. 6, pp. 597–605, 2023.

[23] K. Johnson, V. Arroyos, A. Ferran, R. Villanueva, D. Yin, T. Elberier, A. Aliseda, S. Fuller, V. Iyer, and S. Gollakota, "Solar-powered shape-changing origami microfliers," *Science Robotics*, vol. 8, no. 82, p. eadg4276, 2023.

[24] Z. Yu, J. Tran, C. Li, A. Weber, Y. P. Talwekar, and S. Fuller, "TinySense: A Lighter Weight and More Power-Efficient Avionics System for Flying Insect-Scale Robots," in *2025 IEEE International Conference on Robotics and Automation (ICRA)*, pp. 3839–3845, May 2025.

[25] K. Johnson, Z. Englhardt, V. Arroyos, D. Yin, S. Patel, and V. Iyer, "Millimobile: An autonomous battery-free wireless microrobot," in *Proceedings of the 29th Annual International Conference on Mobile Computing and Networking*, pp. 1–16, 2023.

[26] N. Elkunchwar, S. Chandrasekaran, V. Iyer, and S. B. Fuller, "Toward battery-free free flight: Duty cycled recharging of small drones," in *Int. Conf. Robotics and Intelligent Systems (IROS)*, 2021.